

PHYSICAL SCIENCES

The optical nose: Monolayer sensitization of Au surfaces for plasmonic gas sensing

Elle W. Wyatt¹, Sarah May Sibug-Torres¹, Marika Niihori¹, James W. Beattie¹, Tabitha Jones¹, Nicolas Spiesshofer¹, Jana Hofmann¹, Bart de Nijs², Jeremy J. Baumberg^{1*}

Robust real-time gas sensing is important for many fields, including agriculture and health care analysis of breath/biofluid volatiles. Ammonia is ambiently present at parts per billion (ppb) to parts per million (ppm) levels, but current detection technologies suffer long measurement times, instability, cost, and issues with selectivity. Here, surface-enhanced Raman spectroscopy (SERS) is markedly improved through precision precleaning protocols, which allow surface sensitization of the metal facets using a water monolayer. Harnessing monolayer aggregates of densely packed gold nanoparticles with sub-nanometer spacing defined by rigid scaffolding molecules gives sub-ppm detection of ammonia at room temperature. Accessing the poorly studied high-wave number [>2500 per centimeter (cm^{-1})] region provides much improved discriminatory capabilities, enabling us to generalize this approach to a range of volatile organic carbon (VOC) molecules including ethanol, methanol, and acetone.

INTRODUCTION

The ability to detect gases and volatile organic compounds [volatile organic carbons (VOCs)] at low concentration is of interest in fields from safety, air quality monitoring, climate mitigation, and agriculture to health care (1–6) relevant for COVID, asthma, and diabetes. In most cases, gases and VOCs are present at between parts per million (ppm) and parts per billion (ppb) concentrations, which requires highly sensitive methods for detection.

Ammonia is an analyte of interest for breath analysis for certain types of cancer and kidney disease (present at a few hundred ppb) (7–10) as well as monitoring atmospheric pollution due to industry and agriculture (irritant effects begin at ~ 10 ppm) (11–14). The current gold standard for detection is gas chromatography–mass spectrometry (GC–MS), which is highly sensitive (ppb) (15) but has high complexity, size, and cost (16–18). Aside from GC–MS, current methods of ammonia monitoring are commonly based on electrochemical resistance changes in metal oxides or polymer films, achieving limits of detection (LODs) of 0.1 to 100 ppm (19–21). These approaches also suffer from issues with selectivity, changes in humidity, and long-term stability or reversibility of interactions.

Surface-enhanced Raman spectroscopy (SERS) can offer highly specific and sensitive information about analyte molecules adsorbed at a surface (22, 23), including the analyte structure and its interactions with the surface. SERS can thus deliver an in situ, inexpensive sensing methodology with high sensitivity and specificity for trace gas and VOC detection without the need for preconcentration. SERS has recently gained traction for measuring VOCs using substrates from lithographically fabricated to colloidal nanoparticles, but SERS studies of ammonia detection are not widespread, with previous works focusing mainly on liquid conditions (24, 25). These studied the Raman peaks of ammonia and those originating from ammonia-water interactions but report SERS detection in solution only down to $\text{LOD}_{\text{soln}} \sim 1$ ppm. Raman spectroscopy of gaseous ammonia has been

reported at different temperatures when diluted in nitrogen but without any details on the concentrations (26).

We recently developed a reproducible SERS substrate that exploits the self-assembly of gold nanoparticles (AuNPs) into two-dimensional (2D) close-packed near-monolayer aggregate arrays (“MLaggs”) with precision (0.9 nm) plasmonic nanogaps defined by cucurbit[*n*]uril (CB[*n*], *n* = 5 to 8) molecular spacers (or “scaffolds”) (27–29). Crucially, these substrates can be precision precleaned to remove all organic surfactants and contaminants in their production, and additional cleaning cycles can regenerate the MLAGG sensing surface between uses (27, 28). Even under ambient conditions, a monolayer of water is seen on the AuNP facets (30). Large SERS enhancements (28) ($>10^6$) for molecules in the gaps between AuNPs make MLAGGs ideal for sensing low concentrations of analytes, including in the gas phase. We previously demonstrated SERS sensing of several VOC molecules from the headspace of a volatile in the fingerprint region of 600 to 1800 cm^{-1} using cucurbit[5]uril (CB[5])–scaffolded MLAGGs (27). In the current work, the spectral regions are crucially expanded to include < 450 cm^{-1} , where interactions with gold are seen, and >2800 cm^{-1} , where C–H, N–H, and water O–H peaks arise. With this increased spectral information, the mechanisms that mediate the MLAGG ammonia and VOC sensing can be understood.

In contrast to liquid-based sensing, the water monolayer at the nanoparticle surfaces advantageously acts as a surface sensitization layer for gas sensing using MLAGGs. Ammonia vapor interacts both with this water monolayer, as well as directly with the Au, allowing detection down to a few ppb. Using other nanogap scaffolds and solvents tunes or blocks these interactions. Surface sensitization is also demonstrated for other small VOCs (alcohols and ketones) in the ppm range, heralding the realization of an “optical nose” (31). This clarifies debates about whether vapor sensing is optimized with direct gas adsorption onto a sensor or when predissolved into a solvent and sensed in the liquid phase (32).

RESULTS

Pristine ultraclean AuNP surfaces are formed within immobilized MLAGGs by plasma oxidation, which removes all surfactants and CB[5] molecules and oxidizes the nanoparticle surfaces (Fig. 1A; Materials

Copyright © 2026 The Authors, some rights reserved; exclusive licensee American Association for the Advancement of Science. No claim to original U.S. Government Works. Distributed under a Creative Commons Attribution NonCommercial License 4.0 (CC BY-NC).

Downloaded from <https://www.science.org> at Cambridge University on April 09, 2026

¹NanoPhotonics Centre, Cavendish Laboratory, Department of Physics, JJ Thompson Avenue, University of Cambridge, Cambridge CB3 0US, UK. ²Physics for Sustainable Chemistry Group, Department of Physics, JJ Thompson Avenue, University of Cambridge, Cambridge CB3 0US, UK.

*Corresponding author. Email: jjb12@cam.ac.uk

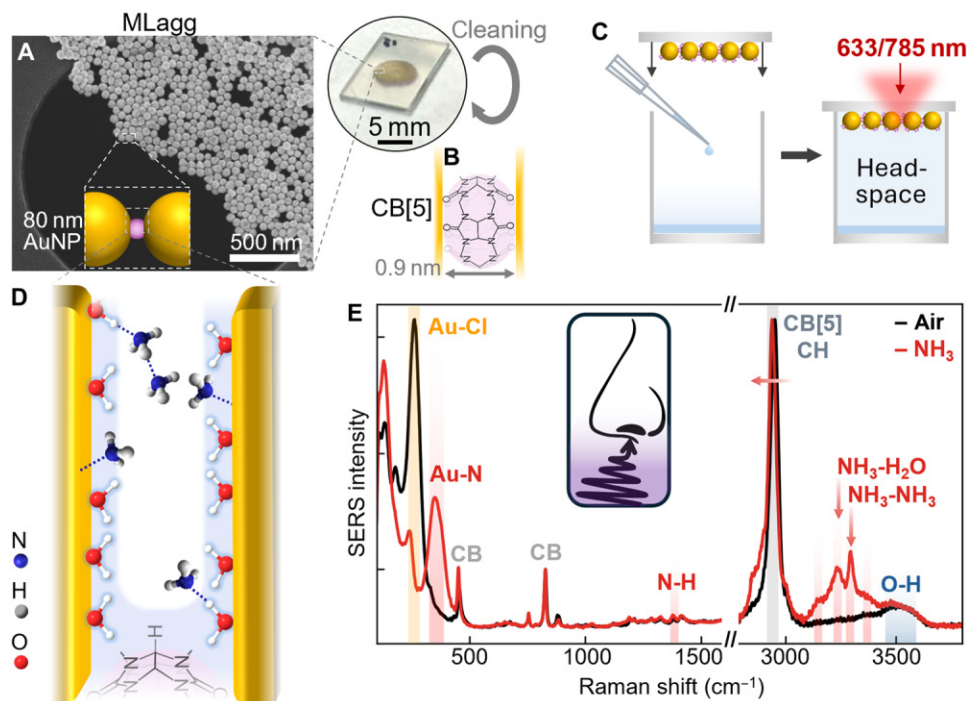


Fig. 1. Multilayer aggregates (MLaggs) for ammonia vapor sensing. (A and B) AuNPs are aggregated with CB[5] and deposited on a coverslip to form a dense film with (B) precisely defined nanogaps. (C) For headspace sensing, 400 μL of 28% ammonia solution is added to a glass vial, which is then sealed with an MLagg-coated coverslip and left for 5 min for the volatile to saturate the headspace. (D) Schematic of the nanogap, identifying different ammonia interactions with the water monolayer and with the Au facets. (E) SERS spectrum of the MLagg in air (black line) and in ammonia vapor (red line), showing the appearance of peaks characteristic to ammonia.

and Methods) (27). A subsequent rescaffolding step reduces the gold oxide, reinserting ligands to scaffold the gap, reforming precision 0.9-nm gaps with high enhancement factors (Fig. 1B). Volatile sensing is performed by placing small volumes of the compound in a sealed chamber, which evaporates and saturates the headspace (Fig. 1C and concentration calculations in section S2 and table S1). MLagg SERS spectra are taken through the supporting coverslip and compared to the spectrum of MLaggs in air (without an analyte).

For MLaggs rescaffolding with CB[5] and measured in a saturated ammonia atmosphere [red line; 450 parts per thousand (ppt)], new peaks appear compared to the same MLagg sample in air (Fig. 1, D and E, black line). Reference sharp peaks at ~450 and 826 cm⁻¹ correspond to the carbonyl portals of CB[5] scaffold molecules and remain unchanged (their binding is unaffected). In the low-wave number region, a strong Au—Cl peak (from the cleaning step) is replaced by a peak at ~340 cm⁻¹ [identified as Au—N in electrochemical cycling of ammonium compounds (33); see below].

Changes are also seen at high wave numbers near water O—H lines (~3500 cm⁻¹) and CB[5] C—H lines (~2900 cm⁻¹). In ammonia vapor, four additional peaks appear between 3000 and 3400 cm⁻¹, two of which are sharper (3293 and 3231 cm⁻¹). Previous Raman studies of ammonia in solution show that the N—H line at 3293 cm⁻¹ comes from hydrogen-bonded NH₃—NH₃, whereas the N—H line at 3231 cm⁻¹ is hydrogen-bonded NH₃—H₂O (24, 25, 34). This latter must form on the water monolayer, with additional NH₃ molecules interacting with the first NH₃ layer (Fig. 1D). Computational studies of ammonia absorption on Au agree that NH₃ can bind either directly to Au atoms or via water molecules absorbed on the surface (35). As well as these new lines, a substantial red shift in the dominant

CB[5] C—H line (of $\Delta\nu = -12.5$ cm⁻¹) and an emerging C—H line at 2865 cm⁻¹ arise, indicating that ammonia changes the CB[5] molecular environment. Similar effects are also seen for CB[6,7]-scaffolded MLaggs in NH₃ vapor (section S1 and fig. S1). Other interactions may occur outside nanogaps but, being outside the SERS hotspots, they are not sensed. These SERS data show that the response of MLaggs to NH₃ vapor is a complex mixture of interactions with the scaffolding CB[5] molecules, the water monolayer in the Au nanogaps, and direct interactions with the Au facets.

To further understand NH₃-MLagg interactions, a headspace concentration series is measured for CB[5] MLaggs, by serially diluting the ammonia solution in the headspace (concentration calculations in section S2, fig. S2, and table S1). As the NH₃ vapor concentration increases from 0 ppb to >400 ppt, gradual changes appear in the MLagg SERS spectra (Fig. 2). Even for low headspace NH₃ concentrations, it is found that the SERS signal saturates within 5 min so the headspace system is at equilibrium (fig. S3).

Characteristic SERS peaks for NH₃ appear in the ppb range, whereas above $c_1 \sim 100$ ppb the CB[5] C—H peak starts shifting to lower energies (Fig. 2, A and E). These effects can be seen in more detail by fitting the peak areas (section S3). Above 100 ppb, two close-spaced peaks (individually identified in fig. S4) at 336 cm⁻¹ (Au—N) and 380 cm⁻¹ [Au⁽⁰⁾—OH] grow (Fig. 2, A, C, and D) with the latter appearing first and the former rising once Au—Cl is removed. At the same time, a Au^(I)—OH peak at 580 cm⁻¹ appears (36), reaching maximum intensity at ~100 ppm.

These data suggest how species rearrange on the AuNP surface, with the Au—Cl first displaced by formation of Au⁽⁰⁾—OH (Fig. 2C, diamonds) and Au^(I)—OH (triangles). Fits to the Langmuir-Hill model

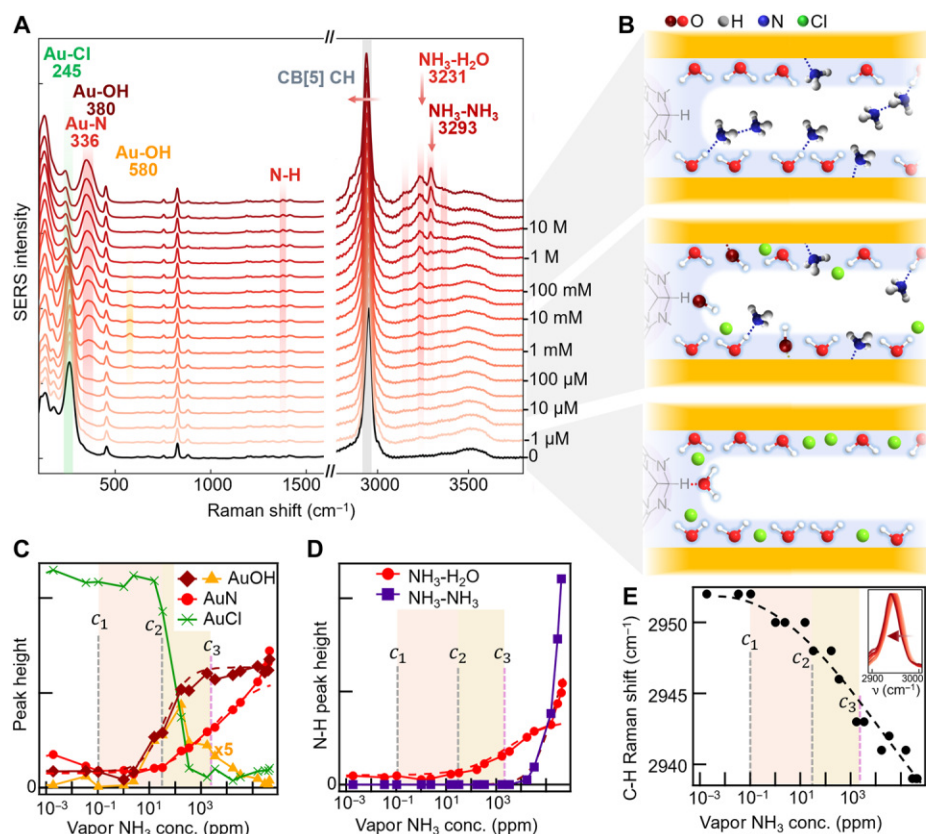


Fig. 2. Headspace concentration series for ammonia sensing. (A) SERS spectra for different added ammonia solution concentrations, with changing peaks shaded. Corresponding headspace concentrations are $1 \mu\text{M} = 2 \text{ ppb}$, $10 \mu\text{M} = 110 \text{ ppb}$, $100 \mu\text{M} = 2.4 \text{ ppm}$, $1 \text{ mM} = 32 \text{ ppm}$, $10 \text{ mM} = 340 \text{ ppm}$, $100 \text{ mM} = 3.5 \text{ ppt}$, $1 \text{ M} = 35 \text{ ppt}$, and $10 \text{ M} = 290 \text{ ppt}$ (see table S1). (B) Schematic configurations in different ammonia sensing regimes identified in concentration series: Initial binding of NH_3 displaces Cl^- ions and forms $\text{Au}-\text{OH}$, followed by the second layer of NH_3 molecules at higher concentrations. (C and D) Extracted peak heights for fits (dashed line) and concentration thresholds c_{1-3} (see Results section). (E) Spectral shift of the CB[5] C–H stretch versus NH_3 concentration.

(dashed line) with $S(c) = S_i [1 + (K/c)^p]^{-1}$ give dissociation constant K and Hill coefficient p for each species. For both $\text{Au}-\text{OH}$ lines, we find $K_{\text{Au}-\text{OH}} \sim 40 \text{ ppm} \equiv c_2$, and $p_{\text{Au}-\text{OH}} \sim 1$ (indicating uncorrelated binding).

The ppb-induced red shifts in the C–H line suggest that OH^- (produced by adding NH_3) hydrogen bonds to the equatorial proton of CB[5] through the dissociation equilibrium $\text{NH}_3 + \text{H}_2\text{O} \leftrightarrow \text{NH}_4^+ + \text{OH}^-$ (Fig. 2B, middle) with $pK_a = 9.25$. This also provides OH^- , which displaces Cl^- ions on Au, maximizing at 100 ppm .

The $\text{Au}-\text{N}$ signal from NH_3 binding (Fig. 2C, circles) rises more slowly ($K_{\text{Au}-\text{NH}_3} \equiv c_3 \sim 3000 \text{ ppm}$ and $p_{\text{Au}-\text{NH}_3} \sim 0.5$). Because $[\text{OH}^-]$, $[\text{NH}_4^+] \propto [\text{NH}_3]^{1/2}$ in this domain (fig. S2), this accounts for $p_{\text{Au}-\text{NH}_3} = 1/2$ if the rate-limiting binding step requires NH_4^+ . Exactly the same rise in the $\text{NH}_3-\text{H}_2\text{O}$ signal is seen (Fig. 2D, circles), implying that NH_4^+ is similarly involved. Because the dynamic range $\Delta \log \text{conc} \approx 4 / (p \ln 10)$ (see section S4 and fig. S5), this range is enhanced by $10^{1/p} = 100$ -fold compared to normal binding. The fall in the $\text{Au}^{(1)}-\text{OH}$ line occurs at the same rate, implying that $\text{Au}-\text{N}$ binding replaces the $\text{Au}-\text{OH}$. This is also consistent with the point at which the concentration of NH_3 exceeds that of OH^- in solution (fig. S2).

At even higher concentrations, the high-wave number N–H peak from NH_3-NH_3 rapidly rises (Fig. 2D, squares) with $K_{\text{NH}_3-\text{NH}_3} \sim$

200 ppt and $p_{\text{NH}_3-\text{NH}_3} \sim 1$. This implies that, once $\text{NH}_3-\text{H}_2\text{O}$ coverage is complete, a second NH_3 layer rapidly forms over the first (Fig. 2B, top). The continuous red shift of the main C–H peak over the whole concentration range (as well as the growth of three shoulder peaks at 2860 , 2900 , and 3000 cm^{-1}) implies that the CH and CH_2 groups on CB[5] interact with the surrounding ions. Of key importance is that these effects span a concentration range of >5 orders of magnitude, a far wider sensor dynamic range than is typical while not suffering from drift (fig. S3). However, we note that, due to this complex range of spectral features and peak shifts, it is not straightforward to use the traditional 3σ analysis to calculate a statistically robust LOD while accounting for all the effects seen. Independent gas-standard calibration with flow measurement should enable this to be quantified in the future.

These effects are highly reproducible when performed for different MLAGG samples (three repeats exactly superimpose; fig. S6A), which is contingent on the precleaning step. Headspace sensing using deuterated solutions (section S5 and figs. S7 and S8) also shows expected red shifts. Comparing $\text{Au}-\text{Cl}$ and $\text{Au}-\text{N}$ peak heights gives relative standard deviation (RSD) between repeats of $\sim 5\%$, which is noteworthy in this field (37).

Comparing vapor (Fig. 2) and liquid sensing (fig. S9) from the same $100 \mu\text{M}$ NH_3 solution show that the headspace $\text{Au}-\text{N}$ peak is five times larger compared to in solution (similar for the N–H peak).

This shows that bulk water competes for nanogap binding sites, thus reducing sensitivity and emphasizing the need for humidity control in precision sensing. It suggests that monolayer water forms a good compromise between direct vapor binding versus presolvation in water.

Apart from monolayer water acting as a surface sensitizer, rescaffolding provides the opportunity to tune MLAGg nanogap chemistry through choice of a rescaffolding ligand. Thiols strongly bind to Au, removing the gold oxide after plasma cleaning without HCl (38). We thus first use 4-mercaptobenzoic acid (MBA), a common SERS pH indicator (39). Comparing MLAGgs with CB[5] and/or MBA (Fig. 3A) shows that direct binding of NH_3 to Au is strongly inhibited by the dense packing of thiol molecules. In addition, NH_3 -induced deprotonation of the MBA is seen by signals switching from 1700 cm^{-1} (COOH stretch) to 1400 cm^{-1} (COO⁻ stretch). Although effects of NH_3 are observed down to ~ 100 ppb (section S6 and fig. S10), this nonspecific (de)protonation is not a signature unique to ammonia (40).

Another approach is to eliminate water from the nanogaps, here using hydrophobic biphenylthiol (BPT) (removing O—H lines at $\sim 3500\text{ cm}^{-1}$; Fig. 3B, black line). In NH_3 vapor, only minimal shifts

in BPT peaks ($<2\text{ cm}^{-1}$) and intensity ratios are seen, and no N—H peaks or Au—N appear (again due to dense thiol packing). A number of other thiol scaffolds were also tested for ammonia sensing (fig. S11), showing either large SERS changes due to protonation and hydrogen bonding as for MBA [e.g., mercaptopyridine (MPY)] or minimal intensity changes and peak shifts similar to BPT [aminothiophenol (ATP) and nitrothiophenol (NTP)]. Similarly, sensitivity is suppressed by soaking CB[5]-scaffolded MLAGgs in dimethyl sulfoxide (DMSO) for 30 min, replacing most surface water even after drying (Fig. 3C, black line) (30, 41). Although headspace NH_3 displaces $\sim 70\%$ DMSO, the Au—N peak is 10-fold weaker than without DMSO. The high-wave number spectrum also changes, with a weaker NH_3 —DMSO peak. Because DMSO is aprotic, NH_3 no longer ionizes and OH⁻ peaks are absent.

Optimal NH_3 detection combines a water monolayer and CB[5] nanogap scaffold. We note that, even at our lowest concentrations of ~ 2 ppb, a background NH_3 signal is observed [see also principal components analysis (PCA); fig. S6], which we believe is due to ambient NH_3 (our LOD is below this). Pre-cleaning is vital for the sensitization

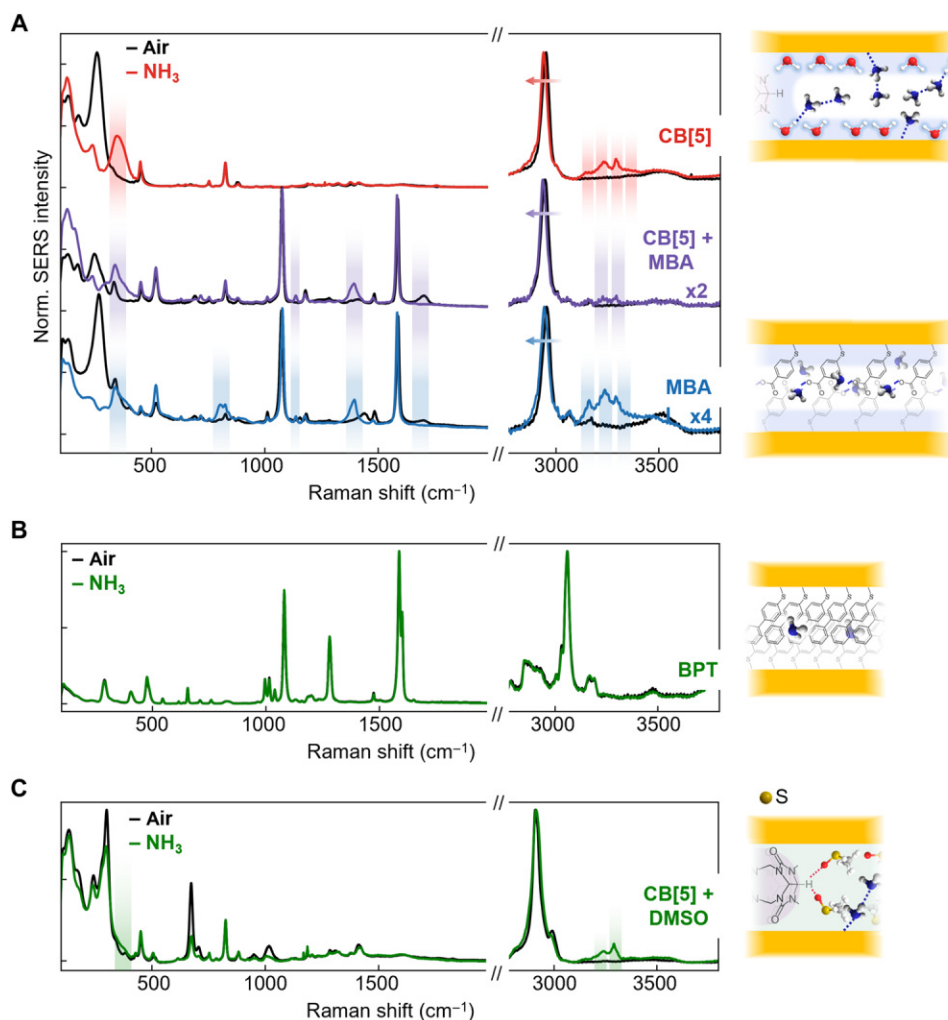


Fig. 3. Effect of different scaffold molecules and nanogap solvents. (A) SERS of MLAGgs rescaffolded with CB[5], CB[5]-MBA, and MBA in air and in a 10 M ammonia headspace, peak changes indicated. (B) MLAGgs rescaffolded with BPT show minimal peak shifts on ammonia binding. (C) Displacement of the water monolayer by DMSO reduces ammonia interactions in the nanogaps. Schematics suggest the possible interactions of ammonia molecules in the nanogaps.

developed here. Using MLaggs without plasma cleaning plus rescaffolding (using NaCl or CB[5] aggregation) gives signals that are extremely weak (section S6 and fig. S12). Citrate remains on these AuNPs, preventing Au–N interactions just as for DMSO. Effective plasma cleaning and surface preparation are thus vital for plasmonic gas sensing applications.

Using this scheme, we now sense other small VOCs relevant for breath/volatile analysis, which are challenging to discriminate in low-cost sensors (concentrations in table S2). Ethanol, methanol, and acetone were selected as commonly available VOCs, with changes in breath concentrations linked to diseases such as lung cancer or diabetes (3, 4). We show improved sensitivities when including the high-wave number C–H and O–H peaks in headspace sensing. In all cases, characteristic analyte molecule peaks appear in the fingerprint region (C=O, C–O, and C–C; fig. S13) (27) along with additional lines between 2800 and 3000 cm^{-1} corresponding to C–H modes of each VOC (Fig. 4, A to D). Characteristic shifts are also seen in the CB[5] C–H peak from all VOCs.

Compared to NH_3 , these analytes produce a greater reduction in intensity and shift of the water monolayer O–H lines to a lower wave number [fig. S13; these O–H peaks correspond to a suppressed hydrogen bonding network (30)]. Decreasing O–H indicates that VOC molecules replace some of the water on AuNP surfaces. No clearly distinguished VOC O–H peaks are seen at $\sim 3400 \text{ cm}^{-1}$ for isopropyl alcohol (IPA), ethanol, and methanol, and nor is any significant VOC–Au bond seen.

Comparison of density functional theory (DFT) calculations of VOC Raman activity to the SERS spectra corroborate this mechanism (section S7 and fig. S14), matching the unique C–H high-wave number lines for each VOC. MLaggs effectively distinguish small volatiles by their C–H lines, using only a narrow waveband (2800 to 3000 cm^{-1}). Large spectral separation ($\lambda \sim 775 \text{ nm}$) from 633-nm Raman lasers and low-cost longpass filters can deliver simple devices, which discriminate these VOCs.

Thiolated scaffolds similarly modify MLagg interactions with VOCs. For BPT-scaffolded MLaggs, sensing of acetone and methanol results in small but repeatable shifts of the major BPT lines (section S8 and fig. S15, A and B). Slightly larger effects are seen for methanol in a triphenylthiol (TPT)-scaffolded MLagg compared to BPT (fig. S15C). This implies that VOCs diffuse into densely packed molecular layers in the nanogaps and perturb their vibrations. Cysteamine-scaffolded MLaggs specifically respond to ketones over alcohols as bridging S–S interactions (42) are formed between neighboring cysteamine molecules. On exposure to VOCs, the S–S peak decreases for ketones (acetone and cyclopentanone) but not for alcohols (ethanol and methanol) (fig. S16A). This is due to hydrogen bonding between the cysteamine

NH_2 and the ketone C=O (43), which forces apart and weakens the S–S links (fig. S16B). The reduction in S–S intensity is related to the number of ketone molecules (30% reduction for 15 ppt cyclopentanone and 65% reduction for 252 ppt acetone). Choosing a nanogap scaffold thus gives selectivity for VOCs with particular functional groups (44).

DISCUSSION

We categorize VOC SERS sensing using precision plasmonic nanocavities depending on in situ interactions (Fig. 5). Analyte molecules (A) either interact directly with the AuNP surfaces, as for NH_3 (Fig. 5A), or with the water monolayer on the Au facets, either by forming hydrogen bonds with the water molecules (as for NH_3), or by partial displacement of the water layer (as for acetone) (Fig. 5B). Such interactions can be blocked when alternate sensitization layers (DMSO) or hydrophobic molecules are used to scaffold the nanogaps (such as for scaffolding $S_i = \text{BPT}$). Binding interactions with scaffold molecules are also possible, to functional groups (as for cysteamine) or different molecule sizes (as for $\text{CB}[n = 5 \text{ to } 8]$) (Fig. 5, C and D, and fig. S1). Multiplexed surfaces with differently functionalized gaps probed in parallel thus have great discriminatory power (44). Understanding these interfacial effects in detail for different VOCs is thus crucial, but for optimal sensor performance, other factors must also be accounted for. These include the effects of temperature and humidity on the Au surface and how to achieve precise humidity or solvent layer control, absorption of analytes into the Au surface [for instance, NH_3 is not known to dissolve Au at room temperature (45)], and competitive binding effects in the nanogaps.

We have shown that precleanable plasmonic surfaces (MLaggs) sense ammonia down to ppb levels, achieving LODs matching GC-MS ($\sim 150 \text{ ppb}$) (15). In contrast to GC-MS, this does not require extensive sample preparation or long measurement times, enabling real-time and in situ measurements. As for GC-MS, Raman spectrometers can currently be bulky and expensive, but there has been much recent progress toward low-cost portable Raman instruments. MLagg interactions with gas molecules are mediated by the AuNP surface and its water monolayer, as well as the nanogap solvent and scaffold molecules. Precleaning/rescaffolding here avoids problems of drift often encountered for current gas sensors while providing quantitative calibration. The dynamics of this optical nose match human olfaction (currently $< 10 \text{ s}$; fig. S17) and potentially can be enhanced. For instance, suspending freestanding MLaggs over open apertures (as they are highly robust; Fig. 1A) allows alternative flow-through geometries that reduce diffusional distances $< 100 \text{ nm}$ and reaction times potentially $< 1 \text{ ns}$ given high flow rates.

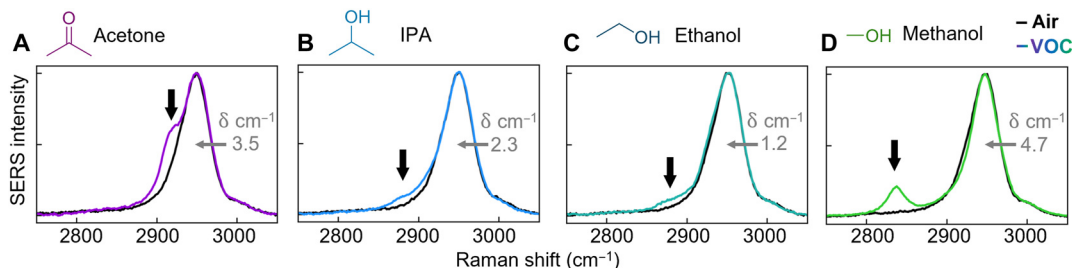


Fig. 4. SERS sensitivity of C–H vibration to VOCs. SERS spectra for MLaggs in air (black lines) and in the headspace of four different VOCs at their undiluted saturation concentrations: (A) acetone (252 ppt), (B) IPA (44 ppt), (C) ethanol (81 ppt), and (D) methanol (1660 ppt), showing the appearance of C–H peaks characteristic to each (arrows). Peak shifts of CB[5] C–H lines as labeled to bring them into registry.

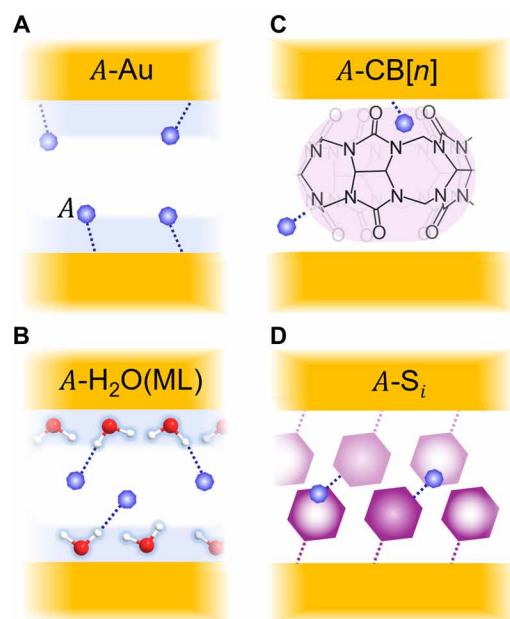


Fig. 5. MLagg gas sensing schemes of analyte A. (A) Direct interaction with AuNP. (B) Interaction with the water monolayer (ML). (C) Interaction/sequestration by CB[n]. (D) Interaction with scaffold molecule (S_i) functional groups.

These interactions can be generalized to other volatile amines, also of interest as VOC analytes (4, 10). Further sensitization of AuNP surfaces is possible, either by using different molecules in the rescaffolding step or by altering the solvent in the nanogaps. This offers the potential to tune the MLagg affinity to different gases. These methods are applicable to a wide range of small VOC molecules, but for future applications, these must be extended to complex VOC mixtures as single VOCs will rarely be present in isolation. This could be achieved using selective MLagg surface sensitizations in different sensor regions to enhance differentiation of mixture components. Detection of VOC mixtures will also require more complex data analysis techniques involving machine learning to resolve overlapping SERS peaks from different VOCs, competitive binding effects, and large datasets. Classification of the observed gas sensing mechanisms demonstrates the versatility and quantitative reliability offered by precleaned MLagg systems, especially for machine learning modalities. Combining these developments opens up robust MLagg-based gas sensors for a diverse range of applications, with optimal surface functionalization chosen to enhance the selectivity and sensitivity of MLagg-based gas and VOC sensing.

MATERIALS AND METHODS

Monolayer aggregate preparation

Five hundred microliters each of chloroform (CHCl₃) and commercial (BBI Solutions) citrate-capped 80-nm AuNPs was added to an Eppendorf tube. One hundred microliters of a 1 mM CB[5] solution was then added and shaken for ~1 min to initiate aggregation. The mixture was left to settle for the immiscible CHCl₃ and aqueous phases to separate and the aggregated AuNPs to move to the interfaces (chloroform-aqueous and aqueous-air). The aqueous phase was washed with three 300- μ l aliquots of deionized (DI) water to dilute the citrate salts and other supernatants and then concentrated by careful removal of the aqueous phase to form an ~5- μ l aggregate droplet floating on the

CHCl₃. The droplet was deposited onto a precleaned sapphire coverslip (0.15 mm thick), which minimizes background fluorescence. Once dried, the resulting AuNP monolayer aggregate (MLagg) was rinsed with DI water and dried with N₂.

The MLaggs were oxygen plasma cleaned for 45 min (oxygen mass flow: 30 standard cubic centimeter per minute; 90% radio frequency power) using a plasma etcher (Diener electronic GmbH & Co. KG) to remove CB[5], citrate, and other supernatants from the AuNP surfaces (verified using SERS). To reintroduce a scaffolding ligand, the MLaggs were immersed in 1 mM CB[5] solution prepared in 0.5 M HCl for 5 min and then rinsed with DI water and dried with N₂.

To rescaffold the MLaggs with thiolated molecules, the samples were plasma cleaned for 45 min as before and then immersed for 30 min in a 10 mM solution of the thiol in ethanol.

All chemicals were purchased from Sigma-Aldrich, and aqueous solutions were prepared in DI water (>18.2 M Ω -cm⁻¹; Purelab Ultra Scientific system).

SERS measurements

SERS measurements were collected on a Renishaw InVivo Raman confocal microscope, using a 20x objective (numerical aperture = 0.4) and a grating of 1200 lines mm⁻¹. To collect the lower-wave number spectral regions, the 785-nm excitation laser was used in extended scan mode, with a 1-s integration time and 0.5% laser power (2.2 mW at the sample).

For MLaggs prepared with 80-nm nanoparticles, the plasmon resonance wavelength occurs at ~800 nm and hence SERS enhancement is optimal for 785-nm laser excitation (27). Use of an edge filter with cutoff at ~100 cm⁻¹ enabled measurement between 100 and 450 cm⁻¹.

A 633-nm laser was used to collect SERS spectra in the region of 2000 to 4000 cm⁻¹, with a 30-s integration time and 10% laser power (0.37 mW at the sample). At these higher Raman shifts (2000 to 4000 cm⁻¹), the SERS light collected by the spectrometer charge-coupled device (CCD) for 785-nm excitation would have $\lambda > 1000$ nm, where the CCD quantum efficiency is poor. Using a 633-nm excitation laser for these measurements shifts our detection light to shorter wavelengths, for better CCD detection efficiency and relatively good MLagg coupling.

All measurements were taken at room temperature, and spectra were calibrated with respect to silicon. Spectra were analyzed using the Python code, and any background was removed by iteratively fitting a polynomial to the base of the peaks. Static measurements were taken at 5 to 10 spots on the MLagg and averaged. Ten measurements taken on the same MLagg have an RSD of ~4%, calculated from the Au–N peak.

Examination of the Stokes: Anti-Stokes ratio indicates that these measurement conditions result in a MLagg temperature rise of <10 K mW⁻¹ (46, 47), and even after repeated exposure over 60 min, the water monolayer remains stable, with the O–H peak remaining at constant intensity (fig. S18) (30).

Headspace sensing

A small volume (~400 μ l) of each volatile compound was added to a 2-ml glass vial, and the upper rim of which had been coated with a layer of “Parafilm M.” The sapphire coverslip holding the rescaffolded MLagg was then gently pressed, MLagg side down, onto the top of the rim of the glass vial to create a sealed chamber. This was left for 5 min for the volatile vapor to saturate the vial environment, and then SERS spectra were taken through the glass coverslip. As the

droplets of volatile compound in the vial never fully evaporate, it can be assumed that the analytes reach saturation concentration (see calculations in section S2 and tables S1 and S2).

To take a headspace ammonia concentration series, serially diluted ammonia solutions were used as the volatile compound, changing the partial pressure of the ammonia and hence the concentration in the headspace (whereas the water vapor concentration remained roughly constant at ~31 ppt; section S2). Measurements were made from low to high headspace concentrations. The MLAGG sample was purged with an ~10-s N₂ flow from a N₂ gun before each subsequent measurement to remove any NH₃ remaining from the previous measurement.

Supplementary Materials

This PDF file includes:

Sections S1 to S8

Figs. S1 to S18

Tables S1 and S2

References

REFERENCES

1. L. D. Lehman-McKeeman, "Absorption, distribution, and excretion of toxicants," in *Casarett & Doull's Essentials of Toxicology, Third Edition* (McGraw-Hill Education, 2015).
2. S. Li, A. Simonian, B. A. Chin, Sensors for agriculture and the food industry. *Electrochem. Soc. Interface* **19**, 41–46 (2010).
3. X. Zhou, Z. Xue, X. Chen, C. Huang, W. Bai, Z. Lu, T. Wang, Nanomaterial-based gas sensors used for breath diagnosis. *J. Mater. Chem. B* **8**, 3231–3248 (2020).
4. A. Sharma, R. Kumar, P. Varadwaj, Smelling the disease: Diagnostic potential of breath analysis. *Mol. Diagn. Ther.* **27**, 321–347 (2023).
5. F. Di Francesco, R. Fuoco, M. G. Trivella, A. Ceccarini, Breath analysis: Trends in techniques and clinical applications. *Microchem. J.* **79**, 405–410 (2005).
6. J. Dummer, M. Storer, M. Swanney, M. McEwan, A. Scott-Thomas, S. Bhandari, S. Chambers, R. Dweik, M. Epton, Analysis of biogenic volatile organic compounds in human health and disease. *Trends Analyt. Chem.* **30**, 960–967 (2011).
7. J. Obermeier, P. Trefz, J. Happ, J. K. Schubert, H. Staude, D.-C. Fischer, W. Miekisch, Exhaled volatile substances mirror clinical conditions in pediatric chronic kidney disease. *PLOS ONE* **12**, e0178745 (2017).
8. C. Turner, P. Spanel, D. Smith, A longitudinal study of ammonia, acetone and propanol in the exhaled breath of 30 subjects using selected ion flow tube mass spectrometry, SIFT-MS. *Physiol. Meas.* **27**, 321–337 (2006).
9. S. Davies, P. Spanel, D. Smith, Quantitative analysis of ammonia on the breath of patients in end-stage renal failure. *Kidney Int.* **52**, 223–228 (1997).
10. P. C. Moura, M. Raposo, V. Vassilenko, Breath volatile organic compounds (VOCs) as biomarkers for the diagnosis of pathological conditions: A review. *Biomed. J.* **46**, 100623 (2023).
11. C. Pinheiro, C. M. Rodrigues, T. Schäfer, J. G. Crespo, Monitoring the aroma production during wine–must fermentation with an electronic nose. *Biotechnol. Bioeng.* **77**, 632–640 (2002).
12. P. Ivanov, E. Llobet, A. Vergara, M. Stankova, X. Vilanova, J. Hubalek, I. Gracia, C. Cané, X. Correig, Towards a micro-system for monitoring ethylene in warehouses. *Sens. Actuators B Chem.* **111–112**, 63–70 (2005).
13. C. Baratto, G. Faglia, M. Pardo, M. Vezzoli, L. Boarino, M. Maffei, S. Bossi, G. Sberveglieri, Monitoring plants health in greenhouse for space missions. *Sens. Actuators B Chem.* **108**, 278–284 (2005).
14. K. E. Wyer, D. B. Kelleghan, V. Blanes-Vidal, G. Schaubberger, T. P. Curran, Ammonia emissions from agriculture and their contribution to fine particulate matter: A review of implications for human health. *J. Environ. Manage.* **323**, 116285 (2022).
15. R. Zaffaroni, D. Ripeti, J. Middelkoop, F. M. Mulder, Gas chromatographic method for in situ ammonia quantification at parts per billion levels. *ACS Energy Lett.* **5**, 3773–3777 (2020).
16. N. H. Snow, Flying high with sensitivity and selectivity: GC–MS to GC–MS/MS. *LCGC N. Am.* **39**, 61–67 (2021).
17. M. Libarioni, P. T. Stevens, J. H. Waite, R. Sacks, Analysis of human breath samples with a multi-bed sorption trap and comprehensive two-dimensional gas chromatography (GC×GC). *J. Chromatogr. B Analyt. Technol. Biomed. Life Sci.* **842**, 13–21 (2006).
18. W. Miekisch, J. K. Schubert, From highly sophisticated analytical techniques to life-saving diagnostics: Technical developments in breath analysis. *Trends Analyt. Chem.* **25**, 665–673 (2006).
19. D. Kwak, Y. Lei, R. Maric, Ammonia gas sensors: A comprehensive review. *Talanta* **204**, 713–730 (2019).
20. M. J. Leferts, M. R. Castell, Ammonia breath analysis. *Sens. Diagn.* **1**, 955–967 (2022).
21. N. Dennler, D. Drix, T. P. A. Warner, S. Rastogi, C. D. Casa, T. Ackels, A. T. Schaefer, A. Van Schaik, M. Schmuker, High-speed odor sensing using miniaturized electronic nose. *Sci. Adv.* **10**, eadp1764 (2024).
22. C. L. Haynes, A. D. McFarland, R. P. Van Duyne, Surface-enhanced Raman spectroscopy. *Anal. Chem.* **77**, 338A–346A (2005).
23. J. Langer, D. J. de Aberasturi, J. Aizpuru, R. A. Alvarez-Puebla, B. Auguie, J. J. Baumberg, G. C. Bazan, S. E. J. Bell, A. Boisen, A. G. Brolo, J. Choo, D. Cialla-May, V. Deckert, L. Fabris, K. Faulds, F. J. G. de Abajo, R. Goodacre, D. Graham, A. J. Haes, C. L. Haynes, C. Huck, T. Itoh, M. Käll, J. Kneipp, N. A. Kotov, H. Kuang, E. C. L. Ru, H. K. Lee, J. F. Li, X. Y. Ling, S. A. Maier, T. Mayerhöfer, M. Moskovits, K. Murakoshi, J. M. Nam, S. Nie, Y. Ozaki, I. Pastoriza-Santos, J. Perez-Juste, J. Popp, A. Pucci, S. Reich, B. Ren, G. C. Schatz, T. Shegai, S. Schlücker, L. L. Tay, K. G. Thomas, Z. Q. Tian, R. P. van Duyne, T. Vo-Dinh, Y. Wang, K. A. Willets, C. Xu, H. Xu, Y. Xu, Y. S. Yamamoto, B. Zhao, L. M. Liz-Marzán, Present and future of surface-enhanced Raman scattering. *ACS Nano* **14**, 28–117 (2020).
24. Y. Liu, T. Asset, Y. Chen, E. Murphy, E. O. Potma, I. Matanovic, D. A. Fishman, P. Atanassov, Facile all-optical method for in situ detection of low amounts of ammonia. *iScience* **23**, 101757 (2020).
25. T. Ujike, Y. Tominaga, Raman spectral analysis of liquid ammonia and aqueous solution of ammonia. *J. Raman Spectrosc.* **33**, 485–493 (2002).
26. C. Yang, D. Ezendeeva, T. Yu, G. Magnotti, Temperature dependent Raman spectra of ammonia ranging from 3150 cm⁻¹ to 3810 cm⁻¹ for combustion applications. *Opt. Express* **29**, 33234–33244 (2021).
27. D. B. Grys, M. Niihori, R. Arul, S. M. Sibug-Torres, E. W. Wyatt, B. de Nijs, J. J. Baumberg, Controlling atomic-scale restructuring and cleaning of gold nanogap multilayers for surface-enhanced Raman scattering sensing. *ACS Sens.* **8**, 2879–2888 (2023).
28. S. M. Sibug-Torres, D.-B. Grys, G. Kang, M. Niihori, E. Wyatt, N. Spiesshofer, A. Ruane, B. De Nijs, J. J. Baumberg, In situ electrochemical regeneration of nanogap hotspots for continuously reusable ultrathin SERS sensors. *Nat. Commun.* **15**, 2022 (2024).
29. M. Niihori, T. Földes, C. A. Readman, R. Arul, D.-B. Grys, B. de Nijs, E. Rosta, J. J. Baumberg, SERS sensing of dopamine with Fe(III)-sensitized nanogaps in recleanable AuNP monolayer films. *Small* **19**, e2302531 (2023).
30. E. W. Wyatt, S. M. Sibug-Torres, R. Arul, M. Niihori, T. Jones, J. W. Beattie, B. de Nijs, J. J. Baumberg, Tracking and controlling monolayer water in gold nanogaps using extreme plasmonic spectroscopy. *Small* **21**, e07013 (2025).
31. C. S. L. Koh, H. K. Lee, X. Han, H. Y. F. Sim, X. Y. Ling, Plasmonic nose: integrating the MOF-enabled molecular preconcentration effect with a plasmonic array for recognition of molecular-level volatile organic compounds. *Chem. Commun.* **54**, 2546–2549 (2018).
32. Y. Obeidat, A. M. Rawashdeh, A. Hammoudeh, R. Al-Assi, A. Dagamseh, Q. Qananwah, Acetone sensing in liquid and gas phases using cyclic voltammetry. *Sci. Rep.* **12**, 11010 (2022).
33. A. C. A. de Vooy, M. F. Mrozek, M. T. M. Koper, R. A. van Santen, J. A. R. van Ven, M. J. Weaver, The nature of chemisorbates formed from ammonia on gold and palladium electrodes as discerned from surface-enhanced Raman spectroscopy. *Electrochem. Commun.* **3**, 293–298 (2001).
34. Y. Liu, E. Murphy, E. O. Potma, I. Matanovic, D. A. Fishman, P. Atanassov, Protocol for rapid ammonia detection via surface-enhanced Raman spectroscopy. *STAR Protoc.* **2**, 100599 (2021).
35. N. A. Rogozhnikov, A study of ammonia adsorption on gold face (111). *Mater. Today Proc.* **31**, 473–475 (2020).
36. J. H. K. Pfisterer, F. Nattino, U. E. Zhumaev, M. Breiner, J. M. Feliu, N. Marzari, K. F. Domke, Role of OH intermediates during the Au oxide electro-reduction at low pH elucidated by electrochemical surface-enhanced Raman spectroscopy and implicit solvent density functional theory. *ACS Catal.* **10**, 12716–12726 (2020).
37. D. Grys, R. Chikkaraddy, M. Kamp, O. A. Scherman, J. J. Baumberg, B. De Nijs, Eliminating irreproducibility in SERS substrates. *J. Raman Spectrosc.* **52**, 412–419 (2021).
38. Y. Xue, X. Li, H. Li, W. Zhang, Quantifying thiol–gold interactions towards the efficient strength control. *Nat. Commun.* **5**, 4348 (2014).
39. F. C. Marques, R. S. Alves, D. P. Dos Santos, G. F. S. Andrade, Surface-enhanced Raman spectroscopy of one and a few molecules of acid 4-mercaptobenzoic in AgNP enabled by hot spots generated by hydrogen bonding. *Phys. Chem. Chem. Phys.* **24**, 27449–27458 (2022).
40. K. S. Bai, Raman spectra of some carboxylic acids. *Proc. Indian Acad. Sci. Sect. A* **11**, 212–228 (1940).
41. K. I. Oh, K. Rajesh, J. F. Stanton, C. R. Baiz, Quantifying hydrogen-bond populations in dimethyl sulfoxide/water mixtures. *Angew. Chem. Int. Ed. Engl.* **56**, 11375–11379 (2017).
42. H. Häkkinen, The gold–sulfur interface at the nanoscale. *Nat. Chem.* **4**, 443–455 (2012).
43. Z. Xie, M. V. Ramakrishnam Raju, P. K. Adhithetty, X.-A. Fu, M. H. Nantz, Effect of thiol molecular structure on the sensitivity of gold nanoparticle-based chemiresistors toward carbonyl compounds. *Sensors* **20**, 7024 (2020).

44. N. Kim, M. R. Thomas, M. S. Bergholt, I. J. Pence, H. Seong, P. Charchar, N. Todorova, A. Nagelkerke, A. Belessiotis-Richards, D. J. Payne, A. Gelmi, I. Yarovsky, M. M. Stevens, Surface enhanced Raman scattering artificial nose for high dimensionality fingerprinting. *Nat. Commun.* **11**, 207 (2020).
45. K. N. Han, M. C. Fuerstenau, Factors influencing the rate of dissolution of gold in ammoniacal solutions. *Int. J. Miner. Process.* **58**, 369–381 (2000).
46. J. Huang, B. de Nijs, S. Cormier, K. Sokolowski, D.-B. Gryns, C. A. Readman, S. J. Barrow, O. A. Scherman, J. J. Baumberg, Plasmon-induced optical control over dithionite-mediated chemical redox reactions. *Faraday Discuss.* **214**, 455–463 (2019).
47. W. H. Skinner, R. L. Sala, K. Sokolowski, I. Blein-Dezayes, N. S. Potter, S. Mosca, B. Gardner, J. J. Baumberg, P. Matousek, O. A. Scherman, N. Stone, An all-in-one nanoheater and optical thermometer fabricated from fractal nanoparticle assemblies. *ACS Nano* **19**, 13779–13789 (2025).
48. C. S. Cragoe, C. H. Meyers, C. S. Taylor, The vapour pressure of ammonia. *J. Am. Chem. Soc.* **42**, 206–229 (1920).
49. Q. Shi, P. Davidovits, J. T. Jayne, D. R. Worsnop, C. E. Kolb, Uptake of gas-phase ammonia. 1. Uptake by aqueous surfaces as a function of pH. *J. Phys. Chem. A* **103**, 8812–8823 (1999).
50. S. L. Clegg, P. Brimblecombe, Solubility of ammonia in pure aqueous and multicomponent solutions. *J. Phys. Chem.* **93**, 7237–7248 (1989).
51. N. Wattanavichean, E. Casey, R. J. Nichols, H. Arnolds, Discrimination between hydrogen bonding and protonation in the spectra of a surface-enhanced Raman sensor. *Phys. Chem. Chem. Phys.* **20**, 866–871 (2018).
52. W. A. Feslings, A. Durban, The vapor pressures, densities, and some derived quantities for acetone. *J. Am. Chem. Soc.* **48**, 2885–2893 (1926).
53. G. S. Parks, B. Barton, Vapor pressure data for isopropyl alcohol and tertiary butyl alcohol. *J. Am. Chem. Soc.* **50**, 24–26 (1928).
54. D. Ambrose, C. H. S. Sprake, Thermodynamic properties of organic oxygen compounds XXV. Vapour pressures and normal boiling temperatures of aliphatic alcohols. *J. Chem. Thermodyn.* **2**, 631–645 (1970).
55. S. W. Benson, G. B. Kistiakowsky, The photochemical decomposition of cyclic ketones. *J. Am. Chem. Soc.* **64**, 80–86 (1942).
56. D. Kos, G. Di Martino, A. Boehmke, B. de Nijs, D. Berta, T. Földes, S. Sangtarash, E. Rosta, H. Sadeghi, J. J. Baumberg, Optical probes of molecules as nano-mechanical switches. *Nat. Commun.* **11**, 5905 (2020).

Acknowledgments

Funding: J.J.B. acknowledges financial support from the European Research Council (ERC) under Horizon 2020 research and innovation programme PICOFORCE (grant agreement no. 883703), Proof-of-concept ReSERS (no. 101212602), and the EPSRC (Cambridge NanoDTC EP/L015978/1, EP/L027151/1, EP/X037770/1, and UKRI1255). S.M.S.-T. is supported by the University of Cambridge Harding Distinguished Postgraduate Scholars Programme. S.M.S.-T. and N.S. acknowledge further support from the EPSRC Grant EP/L015889/1 for the EPSRC Centre for Doctoral Training in Sensor Technologies and Applications and AstraZeneca (MedImmune Ltd.). M.N. is supported by a Gates Cambridge fellowship (OPP1144). B.d.N. acknowledges support from the Royal Society (URF\R1\211162) and the EPSRC (EP/Y008294/1). **Author contributions:** E.W.W. and J.J.B. designed the experiments, which were carried out by E.W.W. S.M.S.-T., M.N., J.W.B., T.J., N.S., J.H., and B.d.N. aided with substrate fabrication and data interpretation. Data analysis was by E.W.W. and J.J.B., and all authors contributed to the manuscript drafting and editing. **Competing interests:** J.J.B., E.W.W., S.M.S.-T., and M.N. acknowledge a published patent: Surface-enhanced spectroscopy substrates, publication no.: WO/2024/199899, 3 October 2024. J.J.B., S.M.S.-T., and T.J. acknowledge a filed patent: Detection method and in-flow Detection Method, UK Patent application no.: 2418909.4, 20 December 2024. The authors declare that they have no other competing interests. **Data, code, and materials availability:** All data and code needed to evaluate and reproduce the results in the paper are present in the paper and/or the Supplementary Materials and on the Cambridge Open Data archive: <https://doi.org/10.17863/CAM.119615>. This study did not generate new materials.

Submitted 2 July 2025

Accepted 6 March 2026

Published 8 April 2026

10.1126/sciadv.aea1478

The optical nose: Monolayer sensitization of Au surfaces for plasmonic gas sensing

Elle W. Wyatt, Sarah May Sibug-Torres, Marika Niihori, James W. Beattie, Tabitha Jones, Nicolas Spiesshofer, Jana Hofmann, Bart de Nijs, and Jeremy J. Baumberg

Sci. Adv. **12** (15), eaea1478. DOI: 10.1126/sciadv.aea1478

View the article online

<https://www.science.org/doi/10.1126/sciadv.aea1478>

Permissions

<https://www.science.org/help/reprints-and-permissions>

Use of this article is subject to the [Terms of service](#)

Science Advances (ISSN 2375-2548) is published by the American Association for the Advancement of Science, 1200 New York Avenue NW, Washington, DC 20005. The title *Science Advances* is a registered trademark of AAAS.

Copyright © 2026 The Authors, some rights reserved; exclusive licensee American Association for the Advancement of Science. No claim to original U.S. Government Works. Distributed under a Creative Commons Attribution NonCommercial License 4.0 (CC BY-NC).